

Colossal Nernst power factor in topological semimetal NbSb₂

Peng Li^{1,2}, Pengfei Qiu^{1,2*}, Qing Xu³, Jun Luo^{1,2}, Yifei Xiong^{1,2}, Jie Xiao¹, Niraj Aryal⁴, Qiang Li^{4,5}, Lidong Chen^{1,2}, and Xun Shi^{1,2*}

¹State Key Laboratory of High Performance Ceramics and Superfine Microstructure, Shanghai Institute of Ceramics, Chinese Academy of Science, Shanghai 200050, China

²Center of Materials Science and Optoelectronics Engineering, University of Chinese Academy of Sciences, Beijing 100049, China

³Key Laboratory of Infrared Imaging Materials and Devices, Shanghai Institute of Technical Physics, Chinese Academy of Sciences, Shanghai 200083, China

⁴Condensed Matter Physics and Materials Science Division, Brookhaven National Laboratory, Upton, New York 11973-5000, USA

⁵Department of Physics and Astronomy, Stony Brook University, Stony Brook, New York 11794-3800, USA

*E-mail: qiupf@mail.sic.ac.cn; xshi@mail.sic.ac.cn

Abstract

Today solid-state cooling technologies below liquid nitrogen boiling temperature (77 K), crucial to quantum information technology and probing quantum state of matter, are greatly limited due to the lack of good thermoelectric and/or thermomagnetic materials. Here, we report the discovery of colossal Nernst power factor of $3800 \times 10^{-4} \text{ W m}^{-1} \text{ K}^{-2}$ under 5 T at 25 K and high Nernst figure-of-merit of $71 \times 10^{-4} \text{ K}^{-1}$ under 5 T at 20 K in topological semimetal NbSb₂ single crystals. The observed high thermomagnetic performance is attributed to large Nernst thermopower and longitudinal electrical conductivity, and relatively low transverse thermal conductivity. The large and unsaturated Nernst thermopower is the result of the combination of highly desirable electronic structures of NbSb₂ having compensated high mobility electrons and holes near Fermi level and strong phonon-drag effect. This discovery opens an avenue for exploring material option for the solid-state heat pumping below liquid nitrogen temperature.

Introduction

Capable of converting heat into electricity and *vice versa* without moving parts and green house emission, thermoelectricity plays an important role in solid state energy harvesting and cooling¹⁻⁴. Current thermoelectric (TE) technologies are largely developed for applications around room temperature (cooling/heating) and above (e.g. waste heat recovery), primarily due to the state-of-the-art TE materials exhibiting large electronic entropy, or a large TE power factor - a measurement of entropy transfer capability⁵. However, there is a demand now for TE applications at low temperatures, especially near or below liquid helium boiling point (4.2 K) heightened by applications in exploring quantum state of matters⁶, quantum information science and technologies⁷, and space science and technologies⁸, among others.

TE refrigeration used today is based on the Peltier effect that has the advantages of accurate and fast temperature control, and nearly maintenance-free. As shown in Fig. 1a, when a longitudinal current flows through a thermopile, a longitudinal temperature gradient is formed, yielding the reduction of temperature at one end of the thermopile. Vast majority of TE devices used today have the longitudinal configurations (Fig. 1a) made of n- and p-type elements connected in series where electrical and thermal resistive contact are primary sources of reduced efficiency⁹⁻¹². A maximum temperature drop of around 70 K has been achieved in typical Bi₂Te₃-based TE devices at room temperature by the Peltier effect⁴. However, such technology is greatly limited at temperatures below liquid nitrogen boiling point (~77 K) due to the lack of high-performance TE materials in the low temperature range (Fig. 1b and 1c). The physical reason behind this phenomenon is understood as follows. It has been argued that a good conventional TE semiconductor usually has a band gap $\sim 10k_B T$ (where k_B is the Boltzmann constant and T is the working temperature)¹³. In order to have it efficiently work below 77 K, the band gap should be less than 66 meV. This leads to the great difficulty of finding the potential high-performance TE materials for Peltier refrigeration in the low temperature range since the semiconductors with band gap less than 66 meV are rare.

Ettingshausen refrigerator is a transverse TE device that provides cooling orthogonal to the applied voltage that greatly simplifies a thermopile structure, in which only the electrical contact is required at colder side of the thermoelectric material that does not require compatible p- and n-type elements, and can reduce the thermal resistance. The Ettingshausen effect is shown in Fig. 1a. When a longitudinal current (along the y - direction) flows through a thermomagnetic material under magnetic field, a transverse temperature gradient (along the x - direction) will be formed, yielding the reduction of temperature at the material's transverse side surface. The cooling efficiency of Ettingshausen refrigeration is determined by material's electrical and thermal transport properties in orthogonal directions, which can be evaluated by a comprehensive parameter named as the Nernst figure-of-merit¹⁴, $z_N = \frac{S_{yx}^2 \sigma_{yy}}{\kappa_{xx}}$, where S_{yx} is the Nernst thermopower, σ_{yy} is the longitudinal electrical conductivity, and κ_{xx} is

the transverse thermal conductivity, and magnetic field is along the z -direction, respectively. In contrast to the longitudinal TE power factor PF ($= S^2\sigma$, where S and σ are the Seebeck thermopower and electrical conductivity along the same direction, respectively), the Nernst power factor $PF_N = S_{yx}^2\sigma_{yy}$ is used to determine the transverse pumping power. Electrons and holes moving in the opposite direction driven by the longitudinal current, can carry both charge and energy in the same transverse direction synergistically under magnetic field, resulting in doubling of transverse temperature gradient. Therefore, semimetals with zero band gap or slightly band overlap are particularly suitable for the Ettingshausen cooling at low temperatures below 77 K.

Although the Ettingshausen effect was discovered in 1886¹⁵, the Ettingshausen refrigeration has progressed far less than Peltier refrigeration. For a long time, the investigation is only limited in a few thermomagnetic materials, such as Bi-Sb alloys^{16,17} and In-Sb alloys¹⁸. The peak z_N values of single-crystalline $\text{Bi}_{97}\text{Sb}_3$ ¹⁶ and $\text{Bi}_{99}\text{Sb}_1$ ¹⁷ are $55\times 10^{-4} \text{ K}^{-1}$ under 1 T and $29\times 10^{-4} \text{ K}^{-1}$ under 0.75 T at 115 K, respectively (Fig. 1b). Recently, the discovery of topological semimetals with high carrier mobility has rejuvenated the investigation of Ettingshausen effect^{19–27}. It is noted that the Dirac-like linear electronic band dispersion near Fermi level in topological semimetals²⁸ can lead to an energy-independent electronic density of states that increases linearly with magnetic field, thus create huge electronic entropy^{20,29}. Indeed, the peak z_N of Dirac semimetal ZrTe_5 was reported to reach $10.5\times 10^{-4} \text{ K}^{-1}$ under 13 T at 120 K²¹. Nodal-line semimetal PtSn_4 has the peak z_N of $8\times 10^{-4} \text{ K}^{-1}$ under 9 T at 10 K²². Most recently, Pan et al. reported an ultrahigh z_N of $265\times 10^{-4} \text{ K}^{-1}$ under 9 T at 11.3 K in single-crystalline Weyl semimetal WTe_2 ²⁷. This value is already much higher than that of Bi-Sb alloys (Fig. 1b), which was recently shown to be also a topological semimetal in specific chemical composition range after all³⁰. These results motivate the discovery of new thermomagnetic materials with high z_N below liquid nitrogen temperature from topological semimetals.

In this work, we report that topological semimetal NbSb_2 single crystal is a promising high-performance thermomagnetic material with a colossal PF_N of $3800\times 10^{-4} \text{ W m}^{-1} \text{ K}^{-2}$ under 5 T at 25 K (Fig.1c) and a high z_N of $71\times 10^{-4} \text{ K}^{-1}$ under 5 T at 20 K (Fig. 1b), much higher than most TE and thermomagnetic materials below 77 K. We found that the performance in NbSb_2 benefits from the combination of nearly identical electron and hole concentrations, high electron/hole carrier mobilities, and additional phonon-drag effect.

Results

Crystal structure. NbSb_2 is a topological semimetal³¹. It crystalizes in centrosymmetric monoclinic structure with the space group of $C_{2/m}$. The schematics of its crystal structure is shown in Fig. 2a. The Nb atom is enclosed in a hendecahedron composed of Sb atoms. The hendecahedrons are connected with each other in the way of face to face along the b -axis and edge to edge along

the c -axis, forming an atomic layer parallel to bc plane. The lattice parameters for NbSb₂ are $a = 10.239 \text{ \AA}$, $b = 3.632 \text{ \AA}$, $c = 8.333 \text{ \AA}$, and $\beta = 120.07^\circ$ ³². Fig. 2b shows the NbSb₂ single crystal grown by the chemical vapor transport method. The NbSb₂ single crystal has a bar-like shape with the length about 7 mm and the width about 1-2 mm. The X-ray characterization performed on the upper surface (Supplementary Fig. 1a) shows that strong (200), (400), and (600) diffraction peaks are observed, indicating the high quality of our NbSb₂ single crystal. Supplementary Fig. 1b shows that Nb and Sb are homogeneously distributed inside the matrix, consistent with the pure phase detected by XRD measurement.

Band structure. Fig. 2c shows the calculated band structure of NbSb₂ with the inclusion of spin-orbit coupling (SOC) effect. The Fermi level crosses the conduction band on the path from L to I and the valence band near L , rendering it a typical semimetal. The energy overlap between conduction band and valence band is about 350 meV. From the Fermi surface (FS) plotted in Fig. 2d, we can identify one electron pocket (blue shell) and one hole pocket (red shell) in the first Brillouin zone. The calculated FS area on the ab plane is comparable to the experimentally measured area from the quantum oscillation measurement³³. A plot showing variation of the calculated FS area with chemical potential and comparison with the experimental value is shown in the Supplementary Fig. 2, with the details shown in Supplementary Note 1. The similarity between the calculated and measured FS areas provides validity to the density functional theory (DFT)-predicted electronic structure. The electron pocket and the hole pocket have nearly the same volume leading to well compensated electrons and holes near the Fermi level. Under orthogonal applied magnetic field and current, the electrons and holes in these pockets moving in the opposite direction along the longitudinal current are deflected in the same transverse direction, which can strengthen the Ettingshausen effect.

Transport properties. Supplementary Figs. 3a-b show the temperature dependences of adiabatic transverse electrical resistivity ρ_{xx} and Hall resistivity ρ_{yx} of single-crystalline NbSb₂ under different magnetic fields B . When $B = 0$, the ρ_{xx} rises with increasing temperature, showing typical metal-like conduction behavior. The ρ_{xx} is $\sim 2 \times 10^{-9} \Omega \text{ m}$ at 5 K, which is about 3-4 orders of magnitude lower than those of typical TE materials for Peltier refrigeration^{4, 34}. Upon applying magnetic field, the ρ_{xx} at temperatures below 100 K is greatly increased, a characteristic feature of topological semimetals^{28, 35}. The magnetoresistance (MR) ratio of single-crystalline NbSb₂ under 9 T at 5 K is $1.3 \times 10^5 \%$, comparable to those of extremely large magnetoresistance (XMR) materials reported before, such as MR = $8.5 \times 10^5 \%$ for NbP under 9 T at 1.85 K³⁶, $4.5 \times 10^5 \%$ for WTe₂ under 14.7 T at 4.5 K³⁵, and $5 \times 10^5 \%$ for PtSn₄ under 14 T at 1.8 K³⁷. Supplementary Fig. 3b shows that the absolute value of Hall resistivity ($|\rho_{yx}|$) firstly decreases with increasing temperature, reaches a minimum at about 100 K, and then increases at higher temperature. Under the same magnetic field, the $|\rho_{yx}|$ is much lower than the ρ_{xx} .

To evaluate the Nernst figure-of-merit, we need to know the longitudinal

conductivity σ_{yy} , which can be calculated by the equation

$$\sigma_{yy} = \frac{\rho_{xx}}{\rho_{xx}\rho_{yy} - \rho_{yx}\rho_{xy}} = \frac{\rho_{xx}}{(\rho_{yy}/\rho_{xx})\rho_{xx}^2 + \rho_{yx}^2} \quad (1)$$

where ρ_{yy} is the longitudinal electrical resistivity. The value of ρ_{yy}/ρ_{xx} is determined by measuring the electrical resistivity along the b -axis (ρ_{xx}) and the electrical resistivity along the c -axis (ρ_{yy}) of a thin square single-crystalline NbSb₂ sample (Supplementary Figs. 4a-b). It seems that the electrical resistivities behavior of NbSb₂ is more anisotropic at low temperatures, but less anisotropic at room temperature. Under the assumption that $-\rho_{xy}$ is equal to ρ_{yx} , the σ_{yy} under different magnetic fields is calculated and shown in Fig. 3a. The σ_{yy} firstly increases with increasing temperature, reaches a maximum, and then decreases with further increasing the temperature. The temperature corresponding to the maximum σ_{yy} is gradually shifted from 35 K under $B = 1$ T to 85 K under $B = 9$ T.

The adiabatic Seebeck thermopower S_{xx} below 100 K is very small under $B = 0$ T (Fig. 3b), with the absolute value $|S_{xx}|$ less than $5 \mu\text{V K}^{-1}$. Below 100 K, it increases modestly with increasing magnetic field, with the peak value around $20 \mu\text{V K}^{-1}$ even under $B = 9$ T. Above 100 K, the $|S_{xx}|$ increases with increasing temperature, but the maximum is still much lower than those of conventional TE materials^{34, 38-40}. Such low S_{xx} values are consistent with the semimetal feature of NbSb₂ (Fig. 2c).

Fig. 3c shows the temperature dependence of adiabatic Nernst thermopower S_{yx} of single-crystalline NbSb₂. Under a magnetic field, the absolute value of S_{yx} initially increases with increasing temperature, reaches the maximum value around 21 K, and then decreases at higher temperatures. Similar behavior is observed when the direction of magnetic field is reversed, with the sign of S_{yx} is reversed accordingly. The maximum S_{yx} is about $616 \mu\text{V K}^{-1}$ under 9 T at 21 K, about thirty times of the maximum S_{xx} . Likewise, as shown in the Supplementary Note 2, the thermal Hall effect has little influence on the S_{yx} measurement.

The adiabatic Nernst power factor $PF_N (= S_{yx}^2\sigma_{yy})$ of single-crystalline NbSb₂ under different magnetic fields is shown in Fig. 3d. The PF_N firstly increases with increasing temperature, reaches a peak around 25 K, and then decreases at higher temperatures. At $B = 1$ T, the PF_N reaches $1750 \times 10^{-4} \text{ W m}^{-1} \text{ K}^{-2}$ at 25 K. As shown in Fig. 1c, this value is already much higher than the best Peltier PF of the TE materials, such as $41 \times 10^{-4} \text{ W m}^{-1} \text{ K}^{-2}$ for Bi₂Te₃³⁴, $75 \times 10^{-4} \text{ W m}^{-1} \text{ K}^{-2}$ for SnSe⁴¹, and $25 \times 10^{-4} \text{ W m}^{-1} \text{ K}^{-2}$ for Mg₃Sb₂³⁴. This result is very encouraging as many permanent magnets can easily provide 1 T magnetic field, thus utilizing single-crystalline NbSb₂ for the Ettingshausen cooling is practically viable. At $B = 5$ T, the PF_N is further enhanced to $3800 \times 10^{-4} \text{ W m}^{-1} \text{ K}^{-2}$ at 25 K. As shown in Fig. 1c, this value is much higher than those of single-crystalline PtSn₄²² and single-crystalline Mg₂Pb²⁶. It is only lower than that for WTe₂, which has the PF_N up to $36000 \times 10^{-4} \text{ W m}^{-1} \text{ K}^{-2}$ under 9 T at 15.9 K²⁷.

Fig. 3e shows the adiabatic transverse thermal conductivity κ_{xx} of single-crystalline NbSb₂ from 5 to 300 K measured by using the four-probe method. At $B = 0$, the κ_{xx} increases with increasing temperature, reaches a peak of 90 W m⁻¹ K⁻¹ around 30 K, and then decreases with further increasing temperature. At 300 K, the κ_{xx} is around 24 W m⁻¹ K⁻¹, which is much higher than those of the TE materials for Peiter refrigeration, such as 1.1 W m⁻¹ K⁻¹ for Bi₂Te₃³⁴, 3.0 W m⁻¹ K⁻¹ for filled skutterudites⁴², and 1.0 W m⁻¹ K⁻¹ for Cu₂Se³⁹. However, it is noteworthy that the peak κ_{xx} of single-crystalline NbSb₂ is lower than those of many thermomagnetic materials for Ettingshausen refrigeration, such as 1290 W m⁻¹ K⁻¹ for single-crystalline NbP under 8 T⁴³, 1586 W m⁻¹ K⁻¹ for single-crystalline TaP under 9 T²⁰, and 215 W m⁻¹ K⁻¹ for single-crystalline WTe₂ under 9 T²⁷. When the magnetic field is applied, the κ_{xx} of single-crystalline NbSb₂ at low temperatures is significantly decreased. As shown in Supplementary Fig. 5, the κ_{xx} at 5 K is 35.9 W m⁻¹ K⁻¹ when $B = 0$ T, but only 2.7 W m⁻¹ K⁻¹ when $B = 1$ T. When the magnetic field is increased to 3 T, the κ_{xx} is further decreased. However, under higher magnetic field, the κ_{xx} is almost unchanged. Such κ_{xx} reduction under magnetic field is caused by the suppression of the contribution of carriers in thermal transports. Moreover, as shown in Supplementary Fig. 6, the estimated isothermal κ_{xx} is slightly smaller than the measured adiabatic κ_{xx} .

The measured κ_{xx} in Fig. 3e is mainly composed of the lattice thermal conductivity κ_l and carrier thermal conductivity κ_e . Under magnetic field, their relationship can be expressed by the empirical formula^{20, 22, 44}

$$\kappa_{xx}(B, T) = \kappa_l(T) + \kappa_e(B, T) = \kappa_l(T) + \frac{\kappa_e(0, T)}{1 + \eta B^s} \quad (2)$$

where η and s are the two factors related to the thermal mobility and scattering mechanism, respectively. The increase of B will suppress the contribution of carriers, which is responsible for the reduction of κ_{xx} under high magnetic field (Fig. 3e). By using Equation (2), the measured κ_{xx} data of NbSb₂ under different B and T are fitted. The fitting results are shown in Supplementary Fig. 5a and Supplementary Table 1. The κ_l increases with increasing temperature, reaching the maximum around 25 K, and then decreases at higher temperature. The maximum is caused by the transition from the $\kappa_l \sim T^3$ dependence at low temperature to $\kappa_l \sim T^{-1}$ dependence at high temperature⁴⁵. Based on the fitted κ_e , the Lorenz number L can be calculated from the Wiedemann-Franz law. As shown in Supplementary Fig. 5b, the L at low temperatures is significantly lower than the Sommerfeld value $L = 2.44 \times 10^{-8}$ W Ω K⁻², indicating the violation of Wiedemann-Franz law. The ratio of the Lorenz number to Sommerfeld value (L/L_0) decreases from around 1 near room temperature to the minimum value of 0.29 at $T = 15$ K, and then increases at lower temperature, reaching 0.59 at 5 K. This trend is similar to the phenomenon found in WP₂ by Jaoui et al.⁴⁶. The violation of WF law might be caused by the inelastic scattering of carriers, while the upturn of L/L_0 below 15 K might be caused by the changed carrier scattering mechanism from the inelastic scattering into the elastic scattering from the impurities.

The adiabatic Nernst figure-of-merit $z_N (= \frac{S_{yx}^2 \sigma_{yy}}{\kappa_{xx}})$ under different magnetic fields is shown in Fig. 3f. The corresponding adiabatic $z_N T$ are shown in Supplementary Fig. 7a. The z_N and $z_N T$ increase with increasing temperature, reach the peak value around 20 K, and then decrease at higher temperature. Due to the enhanced PF_N and the reduced κ_{xx} , the z_N of single-crystalline NbSb₂ is greatly enhanced by magnetic field. A maximum of z_N is $33 \times 10^{-4} \text{ K}^{-1}$ under 1 T at 15 K, which is about six times that of PtSn₄ under 9 T at 15 K²² (Fig. 1b). The z_N is further enhanced to $71 \times 10^{-4} \text{ K}^{-1}$ under 5 T at 20 K, corresponding to the adiabatic $z_N T$ of 0.14 and the isothermal $z_N T$ of 0.16 (Supplementary Fig. 6b). With further increasing the magnetic field, the z_N and $z_N T$ tend to saturate (Supplementary Fig. 7b and Supplementary Fig. 7c). As shown in Fig. 1b, the z_N of single-crystalline NbSb₂ is higher than the Peiter figure-of-merit z of all the TE materials^{34, 38, 40, 41, 47, 48}. It is among the best thermomagnetic materials for Etingshausen refrigeration reported so far. More importantly, the high z_N and $z_N T$ of NbSb₂ appear in the temperature range of 5-30 K (Fig. 1b and Supplementary Fig. 7d), which can well satisfy the requirement of refrigeration below liquid nitrogen temperature.

Potential application. Based on the measured thermomagnetic properties, the maximum temperature difference (ΔT_{max}) and the maximum specific heat pumping power (P_{max}) of the present single-crystal NbSb₂ can be estimated by the following equations^{14, 26}

$$\Delta T_{max} = \frac{1}{2} z_N^{iso} T_c^2 \quad (3)$$

$$P_{max} = \frac{S_{yx}^2 T_c^2 \sigma_{yy} A}{2lm} = \frac{S_{yx}^2 T_c^2 \sigma_{yy}}{2Dl^2} \quad (4)$$

where z_N^{iso} is the isothermal figure-of-merit, T_c is the cold end temperature, l and A are the thickness and cross-sectional area of a cuboid sample along the direction of heat flow, m and D are the mass and density of the sample, respectively. Under $B = 5 \text{ T}$ and $T_c = 25 \text{ K}$, the ΔT_{max} of NbSb₂ single crystal is about 2.0 K. Particularly, in the condition of $B = 5 \text{ T}$ and $T_c = 25 \text{ K}$, the theoretical P_{max} of a cuboid sample with $l = 1 \text{ mm}$ is about 14.2 W g^{-1} , which is much higher than the compression refrigerator with gas refrigerants²⁶ (e.g. $P_{max} = 0.05 \text{ W g}^{-1}$ for He at 5 K, 0.1 W g^{-1} for H₂ at 26 K, and 1.0 W g^{-1} for N₂ at 93 K). Furthermore, the mechanical workability of NbSb₂ single crystal is very good. As shown in Supplementary Fig. 8, it can be easily machined into regular thin square and rectangle without cracking. This can facilitate the fabrication of the classic exponential shape for Etingshausen refrigeration⁴⁹.

Two-carrier model. The large and unsaturated S_{yx} under high magnetic field is indispensable for realizing high PF_N and z_N of thermomagnetic materials. As shown in Fig. 4a, beyond the present NbSb₂, nearly all the reported good thermomagnetic materials possess such character^{19, 20, 22, 26, 27, 50}. NbSb₂ is a semimetal with the Fermi level simultaneously crossing the conduction band and valence band (Fig. 2c). Thus, both electrons and holes will take part in the electrical transports. By using Supplementary Equation (13) and (14), the

electron (or hole) carrier concentration n_e (or n_h), and electron (or hole) carrier mobility μ_e (or μ_h) in NbSb₂ can be obtained by fitting the two-carrier model to the measured transverse resistivity $\rho_{xx}(B)$ and Hall resistivity $\rho_{yx}(B)$. This model can well fit the $\rho_{xx}(B)$ and $\rho_{yx}(B)$ data over 5-300 K (Fig. 4b-c). The n_e and n_h are almost the same with each other $\sim 10^{20}$ cm⁻³ over the entire temperature. Likewise, the inset in Fig. 4d shows that the μ_e and μ_h of single-crystalline NbSb₂ are also comparable over the entire temperature range. In a two-carrier model⁵¹ with constant relaxation time approximation and under the ideal conditions of $n_e = n_h$ and $\mu_e = \mu_h = \bar{\mu}$, the S_{yx} can be expressed as

$$S_{yx} = \frac{\bar{\mu}B}{2} (S_{xx}^h - S_{xx}^e) \quad (5)$$

where S_{xx}^e and S_{xx}^h are the Seebeck thermopower of electrons and holes under the magnetic field B , respectively. The details about how Equation (5) is obtained can be found in Supplementary Note 3. Different from the one-carrier model in which a saturated S_{yx} is observed under large magnetic field, the two-carrier model based on Equation (5) gives an unsaturated S_{yx} when magnetic field increases, this is consistent with the measured S_{yx} *vs.* B behavior of single-crystalline NbSb₂ shown in Fig. 4a.

The inset in Fig. 4d shows that the μ_e and μ_h of single-crystalline NbSb₂ are very large at low temperature, reaching $\mu_e = 2.1$ m²V⁻¹ s⁻¹ and $\mu_h = 1.2$ m²V⁻¹ s⁻¹ at 5 K. These values are comparable with the high mobility found in the extremely large magnetoresistance materials, such as Cd₃As₂ ($\mu_e = 6.5$ m²V⁻¹ s⁻¹ and $\mu_h = 0.5$ m²V⁻¹ s⁻¹ at 10 K)⁵⁰, PtSn₄ ($\mu_e = 7.6$ m²V⁻¹ s⁻¹ and $\mu_h = 7.6$ m²V⁻¹ s⁻¹ at 2 K)²², LaBi ($\mu_e = 2.6$ m²V⁻¹ s⁻¹ and $\mu_h = 3.3$ m²V⁻¹ s⁻¹ at 2 K)⁵². The observed high μ_e and μ_h are also consistent with the Dirac-like band dispersion of NbSb₂ near the Fermi level (Fig. 2c). The large μ_e and μ_h are one important reason for the large S_{yx} of single-crystalline NbSb₂.

In addition, it is instructive to plot $(S_{xx}^h - S_{xx}^e)$ of single-crystalline NbSb₂ under different temperatures and magnetic fields. In Fig. 4e, $(S_{xx}^h - S_{xx}^e)$ shows a local peak at 25 K, which is believed to have a consequence for the observed colossal Nernst power factor. In thermoelectrics, such extra-large thermopower peak at low temperature is usually caused by the phonon-drag effect^{14, 51}. With increasing temperature, the phonons with higher momentum are excited. When the momentum of the long-wave acoustic phonons is similar with that of the carriers on the Fermi surface, the phonon-drag effect occurs, leading to the appearance of a peak in the Seebeck thermopower curve at low temperature. The Seebeck thermopower of a material can be written as $S_{xx} = S_d + S_p$, where S_d is related to the charge carrier diffusion processes and S_p is related to phonons. In a degenerate limit, the S_d usually has linear temperature dependence⁵³. The estimation details of S_{xx}^e and S_{xx}^h are shown in Supplementary Note 4. However, as presented in Supplementary Fig. 9, both S_{xx}^e and S_{xx}^h deviate off the linear temperature dependence below 100 K, indicating the non-negligible S_p in single-crystalline NbSb₂ at low temperatures. By subtracting the S_d from the S_{xx}^e and S_{xx}^h , the S_p^e and S_p^h can be estimated, with the details shown in

Supplementary Note 5. As shown in Fig. 4f, the absolute values of S_p^e and S_p^h show the maxima value of $75 \mu\text{V K}^{-1}$ and $193 \mu\text{V K}^{-1}$ around 25 K, much larger than the S_d^e ($5.4 \mu\text{V K}^{-1}$) and S_d^h ($3.6 \mu\text{V K}^{-1}$) at the same temperature, respectively. Consequently, the synergistic effect of S_p^e and S_p^h greatly improves the total Ettingshausen effect in the single-crystalline NbSb₂. At higher temperature, the phonon-drag effect is quickly weakened since the significantly excited high-frequency phonons lead to the reduction of the relaxation time of long-wave acoustic phonons¹⁴. Thus, the S_p^e and S_p^h are quickly decreased after reaching the maxima values. Above 125 K, the electrical transports are mainly determined by the carrier diffusion process. At this time, the measured S_{yx} is comparable with the theoretical value of $283\bar{\mu}/E_F T$ (Supplementary Fig. 10)⁵⁴, where $E_F = 1200$ K is derived from the relation $E_F = \frac{\hbar^2}{2m} (3\pi^2 n)^{2/3}$ ⁵⁵, with the carrier concentration n equaling to $1.5 \times 10^{20} \text{ cm}^{-3}$ and m equaling to the free electron mass m_0 . These prove that the fitted μ and n in Fig. 4d are reasonable.

Discussion

In summary, we report a colossal Nernst power factor of $3800 \times 10^{-4} \text{ W m}^{-1} \text{ K}^{-2}$ under 5 T at 25 K and a high Nernst figure-of-merit z_N with of $71 \times 10^{-4} \text{ K}^{-1}$ under 5 T at 20 K in single-crystalline NbSb₂. There are a number of factors synergistically contributed to the large and unsaturated Nernst thermopower S_{yx} under magnetic field: 1) a favorable band structure providing nearly identical electron and hole concentrations at Fermi level, 2) extraordinary high electron and hole mobilities benefiting from the Dirac-like dispersion of low energy excitations common to several well-known topological semimetals, and 3) strong phonon-drag effect. The phonon-drag effect derived from our data analysis suggests phonon can play an important role in the transport process of Dirac fermions, which is another interesting phenomenon worth of further investigation. This work provides a new material option for the solid-state heat pumping below liquid nitrogen temperature.

Methods

Sample synthesis. NbSb₂ single crystal was synthesized by chemical vapor transport method in two steps. First, polycrystalline powder was synthesized by solid-state reaction. The niobium powder (alfa, 99.99%) and antimony shot (alfa, 99.9999%) with stoichiometry 1:2 was encapsulated in a vacuum quartz tube and reacted at 1023 K for 48 h. Next, the polycrystalline NbSb₂ powders and 0.3 g iodine were sealed in another vacuum quartz tube. The quartz tube was placed in a horizontal furnace with a temperature gradient for 2 weeks. The hot end temperature and cold end temperature of the quartz tube are 1373 K and 1273 K, respectively. Finally, shiny and bar-like single crystals appear in the cold end of the quartz tube.

Characterization and transport property measurements. The phase composition of the single-crystalline NbSb₂ was characterized by X-ray diffraction (XRD, D/max-2550 V, Rigaku, Japan) and scanning electron microscopy (SEM, ZEISS supra-55, Germany) with an energy dispersive X-ray spectroscopy (EDS, Oxford, UK). The electrical and thermal transport properties of single-crystalline NbSb₂ were measured under the magnetic field by using physical property measurement system (PPMS, Quantum design, USA). The alternating current was used in the electrical conductivity measurement with the purpose to eliminate the thermal Hall effect. The transverse resistivity and Hall resistivity were measured by four-probe method and five-probe method, respectively. The Seebeck thermopower was measured on a standard thermal transport option (TTO) platform. The Nernst thermopower was measured on a modified TTO platform, where the Cu wires for measuring voltage signals were separated from the Cernox 1050 thermometers. All measurements of thermal transport were performed by using four-probe method. The details can be found in the Supplementary Note 6 and Supplementary Figs. 11a-b. The measurement direction was marked in the inset of Fig. 2b, which was the same as that of the Seebeck thermopower. Taking *b*-axis as the *x* direction and *c*-axis as the *y* direction, the magnetic field was applied in the *z* direction perpendicular to the *bc* plane. In addition, via comparing with the thermal conductivity of the sample with and without adhering Cu wires (Supplementary Fig. 12), it is concluded that the Cu wires have little influence on the measurement.

Calculation. First-principles calculations were carried out using Quantum espresso software package⁵⁶ with the lattice parameters given in the materials project⁵⁷. Perdew-Burke-Ernzerhof (PBE) exchange-correlation functional⁵⁸ within the generalized gradient approximation (GGA) and fully relativistic norm-conserving pseudopotentials generated using the optimized norm-conserving Vanderbilt pseudopotentials⁵⁹ were used in the calculations. The primitive Brillouin zone was sampled by using a $10 \times 10 \times 10$ Monkhorst-Pack *k* mesh and a plane-wave energy cut off of 900 eV was used. The Fermi surface calculation was performed on a dense *k* mesh of $41 \times 41 \times 41$ and was visualized by using XCrysDen software⁶⁰. The QE calculations were also verified using the projector-augmented wave (PAW)⁶¹ method as implemented in the Vienna ab initio simulation package (VASP)⁶² which gave similar results.

Data availability

The data generated in this study are provided in the Source Data file.

References

1. Yan, Q. & Kanatzidis, M. G. High-performance thermoelectrics and challenges for practical devices. *Nat. Mater.* **21**, 503-513 (2022).
2. Pei, Y., Shi, X., LaLonde, A., Wang, H., Chen, L. & Snyder, G. J. Convergence of electronic bands for high performance bulk thermoelectrics. *Nature* **473**, 66-69 (2011).

3. Fu, C., Zhu, T., Liu, Y., Xie, H. & Zhao, X. Band engineering of high performance p-type FeNbSb based half-Heusler thermoelectric materials for figure of merit $zT > 1$. *Energy Environ. Sci.* **8**, 216-220 (2015).
4. Mao, J., Chen, G. & Ren, Z. Thermoelectric cooling materials. *Nat. Mater.* **20**, 454-461 (2021).
5. Jiang, B., et al. High-entropy-stabilized chalcogenides with high thermoelectric performance. *Science* **371**, 830-834 (2021).
6. Gröblacher, S., et al. Demonstration of an ultracold micro-optomechanical oscillator in a cryogenic cavity. *Nat. Phys.* **5**, 485-488 (2009).
7. Hornibrook, J. M., et al. Cryogenic Control Architecture for Large-Scale Quantum Computing. *Phys. Rev. Appl.* **3**, 024010 (2015).
8. Collaudin, B. & Rando, N. Cryogenics in space: a review of the missions and of the technologies. *Cryogenics* **40**, 797-819 (2000).
9. Zhang, Q., Bai, S. & Chen, L. Technologies and Applications of Thermoelectric Devices: Current Status, Challenges and Prospects. *J. Inorg. Mater.* **34**, 279-293 (2018).
10. Chu, J., et al. Electrode interface optimization advances conversion efficiency and stability of thermoelectric devices. *Nat. Commun.* **11**, 2723 (2020).
11. Qiu, P., et al. High-Efficiency and Stable Thermoelectric Module Based on Liquid-Like Materials. *Joule* **3**, 1538-1548 (2019).
12. Xing, T., et al. High efficiency GeTe-based materials and modules for thermoelectric power generation. *Energy Environ. Sci.* **14**, 995-1003 (2021).
13. Mahan, G. D. Figure of merit for thermoelectrics. *J. Appl. Phys.* **65**, 1578-1583 (1989).
14. Goldsmid, H. J. *Thermoelectric Refrigeration*. (Plenum Press, Wembley, 1964).
15. v. Ettingshausen, A. & Nernst, W. Ueber das Auftreten electromotorischer Kräfte in Metallplatten, welche von einem Wärmestrome durchflossen werden und sich im magnetischen Felde befinden. *Ann. Phys.* **265**, 343-347 (1886).
16. Cuff, K. F., Horst, R. B., Weaver, J. L., Hawkins, S. R., Kooi, C. F. & Enslow, G. M. The thermomagnetic figure of merit and Ettingshausen cooling in Bi-Sb alloys. *Appl. Phys. Lett.* **2**, 145-146 (1963).
17. Yim, W. M. & Amith, A. Bi-Sb alloys for magneto-thermoelectric and thermomagnetic cooling. *Solid-State Electron.* **15**, 1141-1165 (1972).
18. Madon, B., Wegrowe, J. E., Drouhin, H. J., Liu, X., Furdyna, J. & Khodaparast, G. A. Influence of the carrier mobility distribution on the Hall and the Nernst effect measurements in n-type InSb. *J. Appl. Phys.* **119**, 025701 (2016).
19. Watzman, S. J., et al. Dirac dispersion generates unusually large Nernst effect in Weyl semimetals. *Phys. Rev. B* **97**, 161404(R) (2018).
20. Han, F., et al. Quantized thermoelectric Hall effect induces giant power factor in a topological semimetal. *Nat. Commun.* **11**, 6167 (2020).
21. Wang, P., et al. Giant Nernst effect and field-enhanced transversal $z_N T$ in ZrTe₅. *Phys. Rev. B* **103**, 045203 (2021).

22. Fu, C., et al. Largely suppressed magneto-thermal conductivity and enhanced magneto-thermoelectric properties in PtSn₄. *Research* **2020**, 4643507 (2020).
23. Fu, C., et al. Large Nernst power factor over a broad temperature range in polycrystalline Weyl semimetal NbP. *Energy Environ. Sci.* **11**, 2813-2820 (2018).
24. Liu, W., et al. Weyl Semimetal States Generated Extraordinary Quasi-Linear Magnetoresistance and Nernst Thermoelectric Power Factor in Polycrystalline NbP. *Adv. Funct. Mater.* **32**, 2202143 (2022).
25. Feng, T., et al. Large Transverse and Longitudinal Magneto-Thermoelectric Effect in Polycrystalline Nodal-Line Semimetal Mg₃Bi₂. *Adv. Mater.* **34**, 2200931 (2022).
26. Chen, Z., et al. Leveraging bipolar effect to enhance transverse thermoelectricity in semimetal Mg₂Pb for cryogenic heat pumping. *Nat. Commun.* **12**, 3837 (2021).
27. Pan, Y., He, B., Helm, T., Chen, D., Schnelle, W. & Felser, C. Ultrahigh transverse thermoelectric power factor in flexible Weyl semimetal WTe₂. *Nat. Commun.* **13**, 3909 (2022).
28. Li, Q., et al. Chiral magnetic effect in ZrTe₅. *Nat. Phys.* **12**, 550-554 (2016).
29. Skinner, B. & Fu, L. Large, nonsaturating thermopower in a quantizing magnetic field. *Sci. Adv.* **4**, eaat2621 (2018).
30. Kang, J. S., Vu, D. & Heremans, J. P. Identifying the Dirac point composition in Bi_{1-x}Sb_x alloys using the temperature dependence of quantum oscillations. *J. Appl. Phys.* **130**, 225106 (2021).
31. Lee, S. E., et al. Orbit topology analyzed from π phase shift of magnetic quantum oscillations in three-dimensional Dirac semimetal. *Proc. Natl. Acad. Sci. U.S.A.* **118**, e2023027118 (2021).
32. Furuseth, S. & Kjekshus, A. Arsenides and Antimonides of Niobium. *Nature* **203**, 512-512 (1964).
33. Wang, K., Graf, D., Li, L., Wang, L. & Petrovic, C. Anisotropic giant magnetoresistance in NbSb₂. *Sci. Rep.* **4**, 7328 (2014).
34. Mao, J., et al. High thermoelectric cooling performance of n-type Mg₃Bi₂-based materials. *Science* **365**, 495-498 (2019).
35. Ali, M. N., et al. Large, non-saturating magnetoresistance in WTe₂. *Nature* **514**, 205-208 (2014).
36. Shekhar, C., et al. Extremely large magnetoresistance and ultrahigh mobility in the topological Weyl semimetal candidate NbP. *Nat. Phys.* **11**, 645-649 (2015).
37. Mun, E., Ko, H., Miller, G. J., Samolyuk, G. D., Bud'ko, S. L. & Canfield, P. C. Magnetic field effects on transport properties of PtSn₄. *Phys. Rev. B* **85**, 035135 (2012).
38. Liang, J., et al. Crystalline Structure-Dependent Mechanical and Thermoelectric Performance in Ag₂Se_{1-x}S_x System. *Research* **2020**, 6591981 (2020).
39. Liu, H., et al. Copper ion liquid-like thermoelectrics. *Nat. Mater.* **11**, 422-425 (2012).

40. Wang, L., et al. Discovery of low-temperature GeTe-based thermoelectric alloys with high performance competing with Bi₂Te₃. *J. Mater. Chem. A* **8**, 1660-1667 (2020).
41. Qin, B., et al. Power generation and thermoelectric cooling enabled by momentum and energy multiband alignments. *Science* **373**, 556-561 (2021).
42. Shi, X., et al. Multiple-Filled Skutterudites: High Thermoelectric Figure of Merit through Separately Optimizing Electrical and Thermal Transports. *J. Am. Chem. Soc.* **133**, 7837-7846 (2011).
43. Stockert, U., et al. Thermopower and thermal conductivity in the Weyl semimetal NbP. *J. Phys.: Condens. Matter* **29**, 325701 (2017).
44. Ocaña, R. & Esquinazi, P. Thermal conductivity tensor in YBa₂Cu₃O_{7-x}: Effects of a planar magnetic field. *Phys. Rev. B* **66**, 064525 (2002).
45. Ashcroft, N. W. & David, M. N. *Solid state physics*. (Saunders College Publishing, New York, 1976).
46. Jaoui, A., et al. Departure from the Wiedemann–Franz law in WP₂ driven by mismatch in T-square resistivity prefactors. *npj Quantum Mater.* **3**, 64 (2018).
47. Lenoir, B., Cassart, M., Michenaud, J. P., Scherrer, H. & Scherrer, S. Transport properties of Bi-RICH Bi-Sb alloys. *J. Phys. Chem. Solids* **57**, 89-99 (1996).
48. Xu, Q., et al. Thermoelectric properties of phosphorus-doped van der Waals crystal Ta₄SiTe₄. *Mater. Today Phys.* **19**, 100417 (2021).
49. Scholz, K., Jandl, P., Birkholz, U. & Dashevskii, Z. M. Infinite stage Ettingshausen cooling in Bi-Sb alloys. *J. Appl. Phys.* **75**, 5406-5408 (1994).
50. Xiang, J., et al. Large transverse thermoelectric figure of merit in a topological Dirac semimetal. *Sci. China: Phys., Mech. Astron.* **63**, 237011 (2019).
51. Delves, R. T. Figure of merit for Ettingshausen cooling. *Br. J. Appl. Phys.* **15**, 105-106 (1964).
52. Sun, S., Wang, Q., Guo, P., Liu, K. & Lei, H. Large magnetoresistance in LaBi: origin of field-induced resistivity upturn and plateau in compensated semimetals. *New J. Phys.* **18**, 082002 (2016).
53. Blatt, F. J., Schroeder, P. A., Foiles, C. L. & Greig, D. *Thermoelectric power of metals*. (Plenum Press, New York and London, 1976).
54. Behnia, K. & Aubin, H. Nernst effect in metals and superconductors: a review of concepts and experiments. *Rep. Prog. Phys.* **79**, 046502 (2016).
55. Gould, H. & Tobochnik, J. *Statistical and Thermal Physics with Computer Application*. (Priceton University Press, Priceton, 2010).
56. Giannozzi, P., et al. QUANTUM ESPRESSO: a modular and open-source software project for quantum simulations of materials. *J. Phys.: Condens. Matter* **21**, 395502 (2009).
57. Jain, A., et al. Commentary: The Materials Project: A materials genome approach to accelerating materials innovation. *APL Mater.* **1**, 011002 (2013).
58. Perdew, J. P., Burke, K. & Ernzerhof, M. Generalized Gradient Approximation Made Simple. *Phys. Rev. Lett.* **77**, 3865-3868 (1996).

59. Hamann, D. R. Optimized norm-conserving Vanderbilt pseudopotentials. *Phys. Rev. B* **88**, 085117 (2013).
60. Kokalj, A. XCrySDen—a new program for displaying crystalline structures and electron densities. *J. Mol. Graphics Modell.* **17**, 176-179 (1999).
61. Blöchl, P. E. Projector augmented-wave method. *Phys. Rev. B* **50**, 17953-17979 (1994).
62. Kresse, G. & Hafner, J. Ab initio molecular dynamics for liquid metals. *Phys. Rev. B* **47**, 558-561 (1993).

Acknowledgements

This work is supported by the National Natural Science Foundation of China (91963208, L.C. and 52122213, P.Q.), and Shanghai Government (20JC1415100, X.S.). This work at Brookhaven National Laboratory was supported by U.S. Department of Energy (DOE) the Office of Basic Energy Sciences, Materials Sciences and Engineering Division under Contract No. DE-SC0012704.

Author contributions

P.L., P.Q., and X.S. designed the experiment. P.L. synthesized the samples and performed the transport property measurements, with the help of Q.X. and J.X., and N.A. provided band structure calculations. P.L., Q.X., J.L., and Y. X. analyzed the transport properties based on the two-carrier model. P.L., P.Q., Q.L., L.C., and X.S. analyzed the data and wrote the manuscript.

Competing interests

The authors declare no competing interests.

Figures

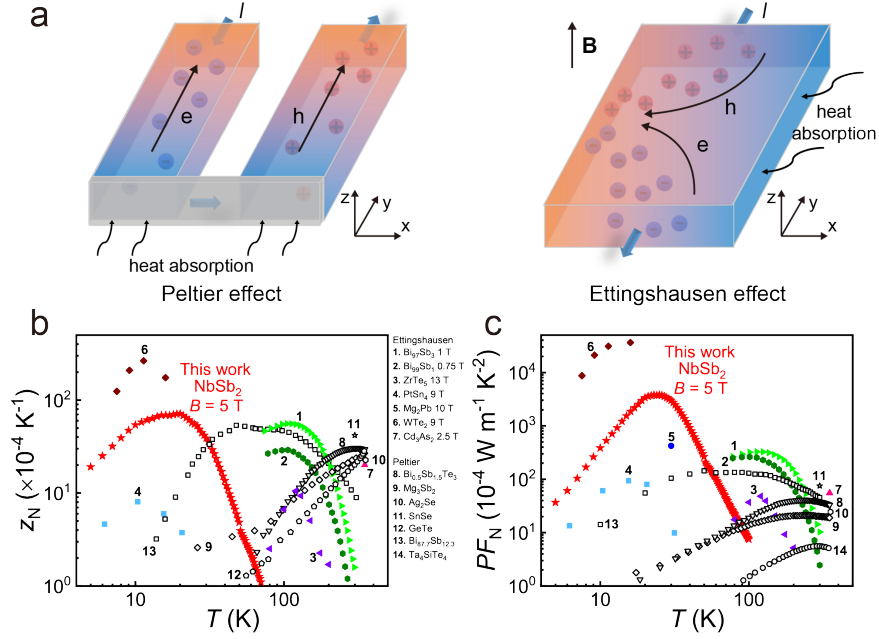


Figure 1. **Peltier effect and Ettingshausen effect.** **a** Schematic diagrams of the Peltier effect and Ettingshausen effect. Comparison of **b** the Nernst figure-of-merit (z_N) and **c** Nernst power factor (PF_N) for single-crystalline NbSb_2 and other thermomagnetic materials^{16, 17, 21, 22, 26, 27, 50}. The Peltier figure-of-merit (z) and Peltier power factor (PF) of typical TE materials are also included^{34, 38, 40, 41, 47, 48}.

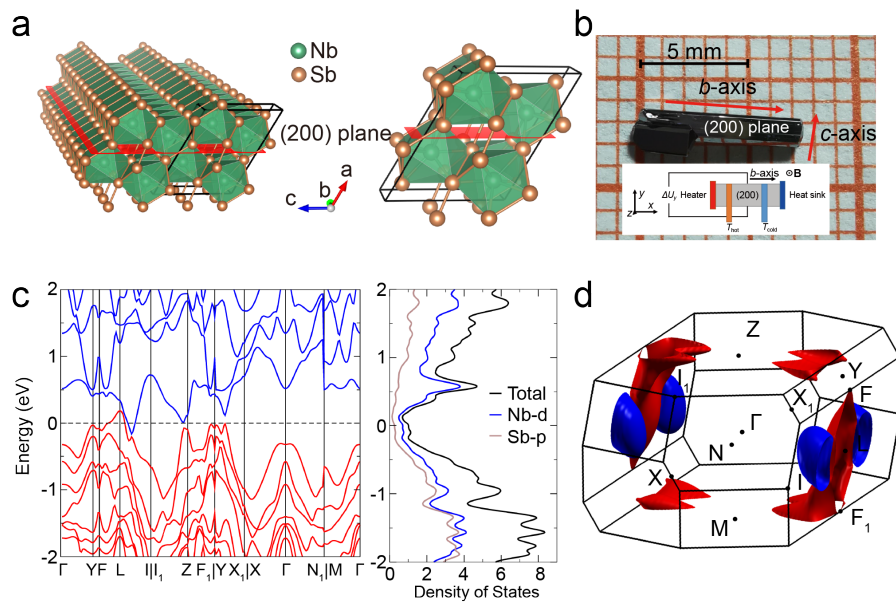


Figure 2. **Crystal structure and band structure of NbSb₂.** **a** Crystal structure of NbSb₂ from different perspectives. **b** Optical image of NbSb₂ single crystal grown in this work. The inset shows the measurement direction of Nernst thermopower. **c** Calculated band structure, density of states, and **d** Fermi surface with the spin-orbit coupling (SOC) for NbSb₂. The red and blue pockets denote the hole and electron pockets, respectively.

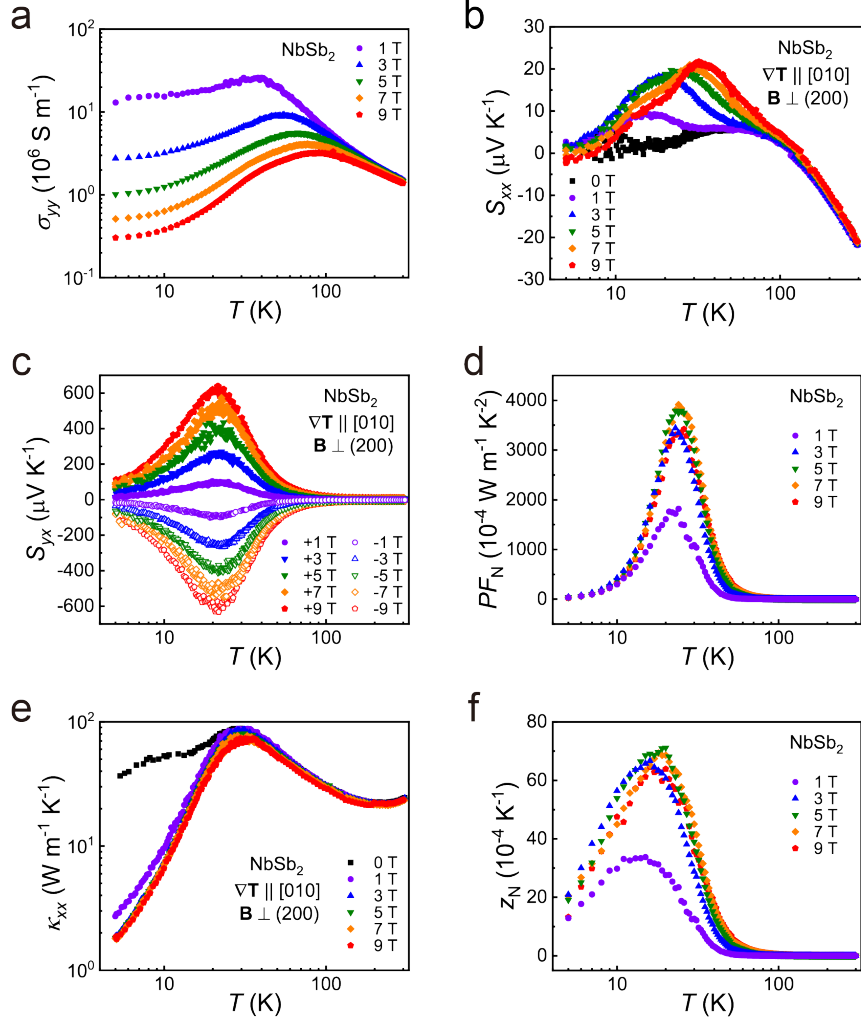


Figure 3. **Electrical and thermal properties of NbSb₂ for Etingshausen refrigeration.** Temperature dependences of **a** electrical conductivity (σ_{yy}), **b** Seebeck thermopower (S_{xx}), **c** Nernst thermopower (S_{yx}), **d** Nernst power factor (PF_N), **e** transverse thermal conductivity (κ_{xx}), and **f** Nernst figure-of-merit (z_N) of single-crystalline NbSb₂ under different magnetic fields and adiabatic condition. In thermal transport measurements, the temperature gradient $\nabla\mathbf{T}$ is parallel to the [010] direction and the magnetic field \mathbf{B} is perpendicular to the (200) plane.

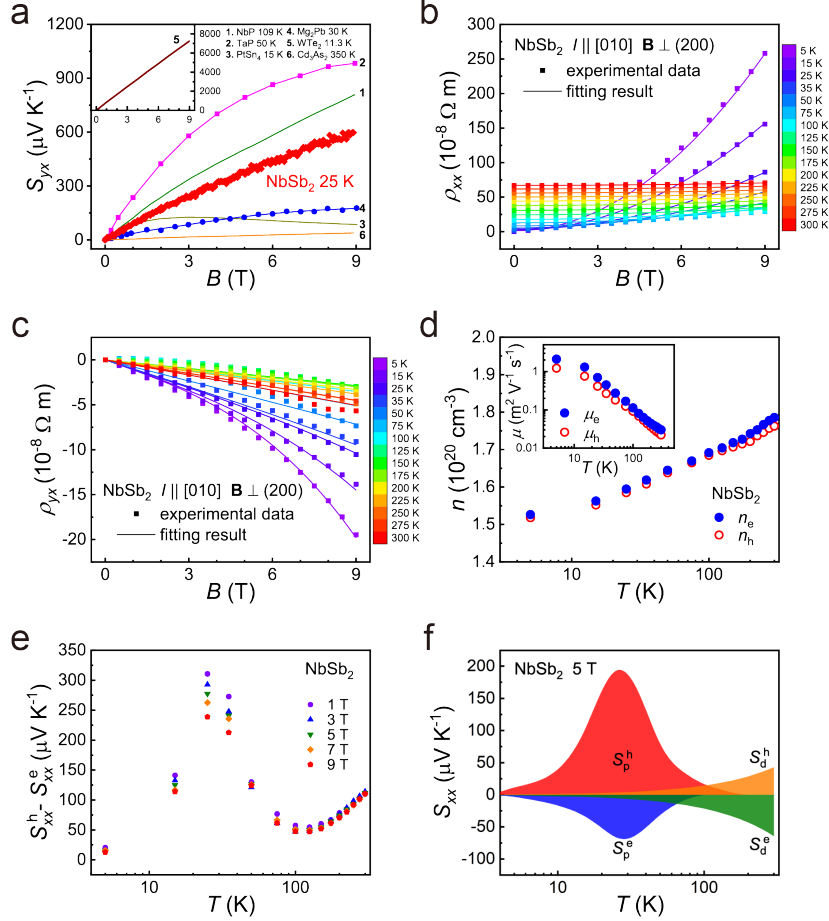


Figure 4. **Detailed electrical transports for NbSb₂ single crystal.** **a** Nernst thermopower (S_{yx}) of single-crystalline NbSb₂ as a function of magnetic field B at 25 K. The data for PtSn₄²², Cd₃As₂⁵⁰, Mg₂Pb²⁶, NbP¹⁹, TaP²⁰, and WTe₂²⁷ are included for comparison. **b** Fitting of the transverse resistivity $\rho_{xx}(B)$ and **c** Hall resistivity $\rho_{yx}(B)$ of single-crystalline NbSb₂ under different temperatures. The symbols are experimental data and the lines are the fitting curves. In electrical transport measurements, the current I is parallel to the [010] direction and the magnetic field \mathbf{B} is perpendicular to the (200) plane. **d** Carrier concentrations (n_e and n_h) and carrier mobilities (μ_e and μ_h) of single-crystalline NbSb₂. **e** Temperature dependence of the difference between Seebeck thermopower of electrons and holes ($S_{xx}^h - S_{xx}^e$) of single-crystalline NbSb₂ under different magnetic fields. **f** Seebeck thermopower of electrons and holes related to the charge carrier diffusion processes (S_p^e and S_p^h) and phonons (S_d^e and S_d^h) at 5 T, respectively.